Article

Disrupting fumarylacetoacetate hydrolase by stratified nanoplatforms orchestrated metabolic-immune reprogramming and prevent post-ablation HCC relapse

Zhiwen Hong[#, 1], Xiaolong Liu[#, 2], Rouhan A[#, 1], Zengzhen Chen[#, 3], Qianjiang Wu[1], Jixian Fu[1, 4], Xue Guan[5], Can Wang[6], Xinghua Wang[1], Shan Jiang[1], Bolong Li[1], Zhaobo Wang[1], Lei Zhang[*, 7], Xianwei Meng[*, 3], Yali Cui[*, 1], Tengchuang Ma[*, 1].

Affiliations:

[1] Department of Nuclear Medicine, Harbin Medical University Cancer Hospital, Harbin 150081, China.

[2] Department of Interventional Radiology, Harbin Medical University Cancer Hospital, Harbin 150081, China.

[3] State Key Laboratory of Cryogenic Science and Technology, Technical Institute of Physics and Chemistry, Chinese Academy of Sciences, Beijing, 100190, China.

[4] Department of Interventional Radiology, the First Hospital of China Medical University, Shenyang, 110001, China.

[5] Animal Laboratory Center, The Second Affiliated Hospital of Harbin Medical University, Harbin 150081, China.

[6] Department of Gynecologic Oncology, Harbin Medical University Cancer Hospital Harbin, Heilongjiang 150081, China.

[7] Department of Interventional Ultrasound, Harbin Medical University Cancer Hospital, Harbin 150081, China.

[#] These authors contributed equally: Zhiwen Hong, Xiaolong Liu, Rouhan A, Zengzhen Chen

[*] Corresponding author: Tengchuang Ma; Yali Cui; Xianwei Meng; Lei Zhang.

[*] **Email:**

matengchuang1988@126.com (T. M.);

yalicui68@126.com (Y. C.);

mengxw@mail.ipc.ac.cn (X. M.);

tianwang.3000@163.com (L. Z.).

Keywords:

microwave ablation therapy; metabolic-immune reprogramming; hepatocellular carcinoma recurrence; nano deliver systems.

Extended Data Figures

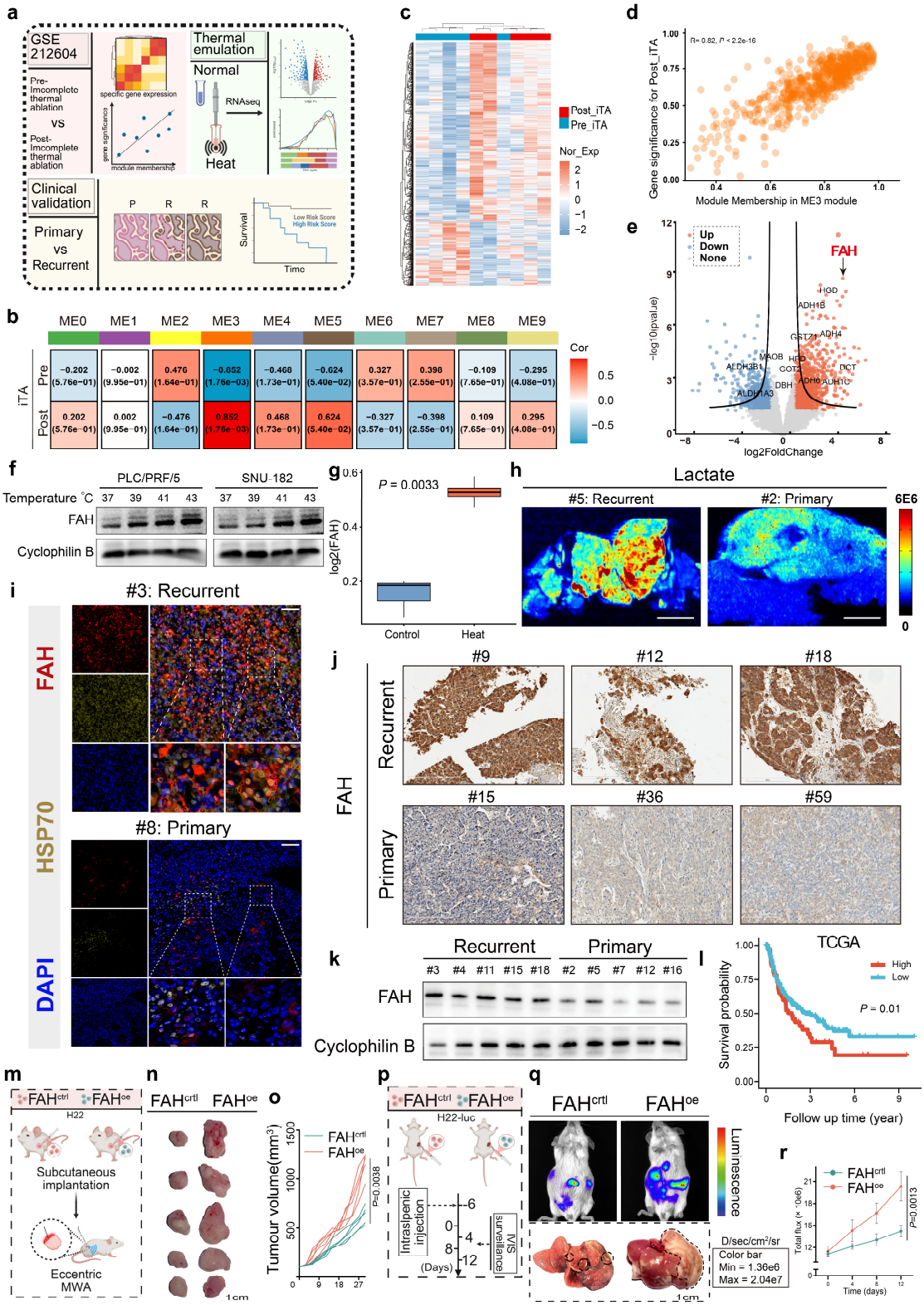

Extended Data Fig. 1 | Thermal ablation induces FAH upregulation and promotes HCC recurrence

a. Schematic of candidate gene screening strategy using GSE212604, clinical samples and heat-treated cell lines.

b. Correlation between gene modules and microwave ablation response identified by WGCNA

(GEO: GSE212604).

c. Expression of selected genes from module ME3, stratified by pre- and post-incomplete microwave ablation status.

d. Correlation between gene significance and module membership in ME3 (R = 0.82).

e. Volcano plot of differentially expressed genes pre- versus post-MWA in HCC patients, highlighting significant FAH upregulation.

f. Western blot analysis of FAH protein expression in PLC/PRF/5 and SNU-182 cells under escalating thermal stress (37 °C to 43 °C).

g. RNA-seq quantification of FAH expression in control (37 °C) versus heat-treated (43 °C) cells.

h. Representative mass spectrometry images showing spatial lactate distribution in cohort 1. Scale bar, 2 mm.

i. Immunofluorescence co-staining of FAH and HSP70 in clinical HCC specimens (cohort 2). Scale bars, 50 μm.

j. Representative IHC staining of FAH in primary and recurrent HCC tissues (cohort 3). Scale bars, 200 μm (n = 108).

k. Western blot analysis of FAH expression in primary and recurrent HCC tissues (cohort 4; n = 3 biological replicates).

l. Kaplan–Meier survival analysis of TCGA-LIHC cohort stratified by FAH expression, showing poorer prognosis with high FAH.

m. Schematic of the relapse HCC model in BALB/c mice using FAH-overexpression (FAH^{oe}) and control (FAH^{ctrl}) H22 cells.

n, o. Representative tumour images **(n)** and growth curves **(o)** of the relapse model groups. Scale bars, 1 cm (n = 5 mice per group).

p. Schematic of the HCC model established via intrasplenic injection of FAH^{oe} and FAH^{ctrl} H22-luc cells in BALB/c mice.

q, **r**. Representative bioluminescence images **(q)** and total flux measurements **(r)** of the intrasplenic HCC model. Scale bars, 1 cm (n = 5 mice per group).

Data are presented as mean ± S.D. from n biologically independent samples (**o, r,** n = 5). Statistical significance was analysed by one-way ANOVA with Sidak's multiple comparisons test for **o, r**. Panels **a, m, p** created with BioRender.com.

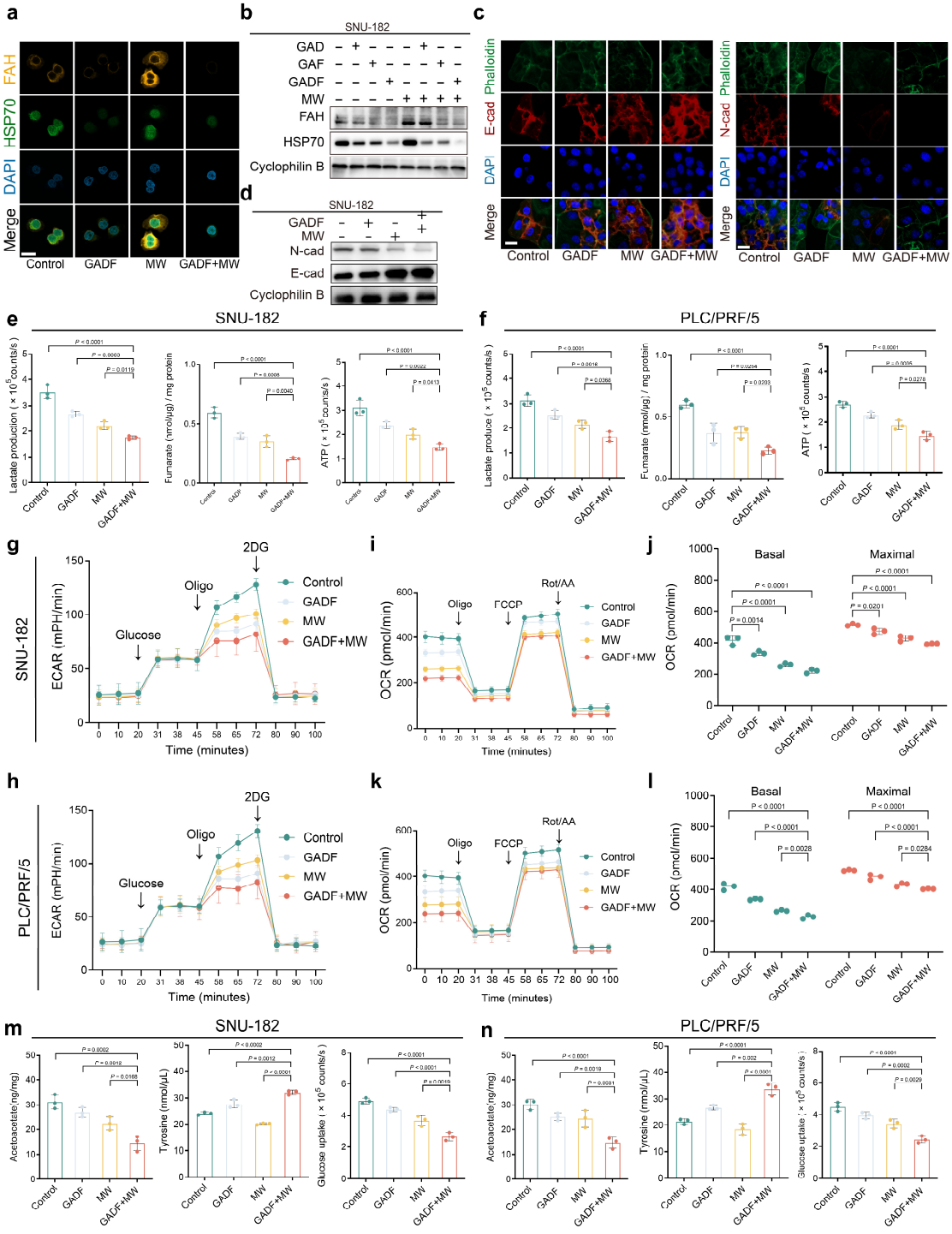

Extended Data Fig. 2 | Therapeutic mimicry of FAH knockdown via GADF induces metabolic reprogramming

a. Immunofluorescence images of FAH and HSP70 in SNU-182 cells across four treatment groups (Control, GADF, MW, GADF + MW). Scale bar, 20 μm (n = 3 biological replicates).

b. Protein expression levels of FAH and HSP70 in SNU-182 cells under eight treatment conditions (Control, GAD, GAF, GADF, MW, GAD + MW, GAF + MW, GADF + MW; n = 3 replicates).

c. Immunofluorescence images of E-cadherin and N-cadherin in SNU-182 cells (Control, GADF, MW, GADF + MW). Scale bar, 20 μm (n = 3 replicates).

d. Protein expression levels of N-cadherin and E-cadherin in SNU-182 cells across indicated groups

(n = 3 replicates).
e, f. Lactate production, intracellular fumarate concentration and ATP production rates in SNU-182 **(e)** and PLC/PRF/5 **(f)** cells under different treatments.
g. ECAR of SNU-182 cells across indicated treatments.
h. ECAR of PLC/PRF/5 cells under indicated conditions.
i. OCR of SNU-182 cells under different treatments.
j. Basal and maximal OCR rates in SNU-182 cells across indicated groups.
k. OCR of PLC/PRF/5 cells under indicated treatments.
l. Basal and maximal OCR in PLC/PRF/5 cells across indicated groups.
m, n. Concentrations of acetoacetate and tyrosine, and glucose uptake rate in SNU-182 **(m)** and PLC/PRF/5 **(n)** cells from the indicated groups.
Data are presented as mean ± S.D. from n biologically independent samples (**e, f, j, l, m, n**; n = 3). Statistical significance was analysed by one-way ANOVA with Dunnett's multiple comparisons test for **e, f, m, n** and two-way ANOVA with Dunnett's test for **j, l**. ns, not significant. Dunnett's test compared each group against the last group.

Supplementary Figures

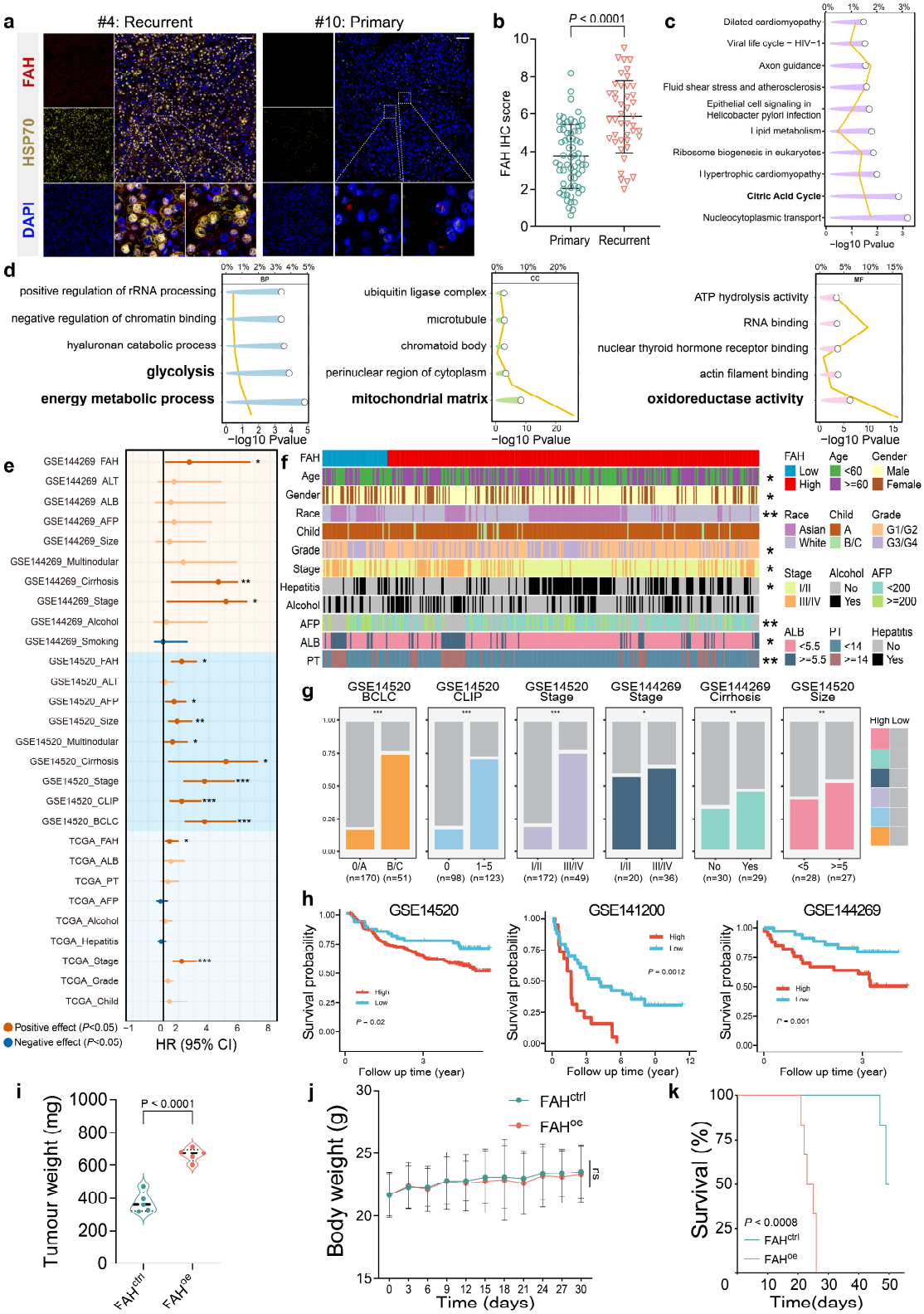

Supplementary Fig. 1 | Thermal ablation induces FAH upregulation and is associated with poor outcomes in HCC. Related to Extended Data Fig. 1.

a, Representative co-immunofluorescence images of FAH and HSP70 in human HCC specimens from Cohort 2. Scale bars, 50 μm.

b, IHC score of FAH expression corresponding to Extended Data Fig. 1j.

c, d, Pathway enrichment analysis of RNA-seq data showing cancer-related biological pathways and metabolic processes. KEGG pathways are presented in (**c**), and GO biological processes in (**d**).
e, Cox univariate regression analysis of risk factors in hepatocellular carcinoma patients across multiple cohorts (TCGA, GSE144269, GSE14520).
f, g, Comparison of clinical characteristics among HCC patients in the GSE14520 and GSE144269 datasets (**f**), with corresponding quantitative analysis (**g**).
h, Kaplan-Meier survival analysis based on FAH expression levels in the GSE14520, GSE141200, and GSE144269 cohorts.
i, Terminal tumour weights from the indicated treatment groups in the relapse model (related to Extended Data Fig. 1m).
j, Body weight curves of mice in the indicated treatment groups (related to Extended Data Fig. 1m).
k, Kaplan-Meier survival curves of mice in the indicated treatment groups (related to Extended Data Fig. 1m).
Data are presented as mean ± s.d. from *n* biologically independent samples (**b,** $n = 108$; **i-k,** $n = 5$). Statistical significance was analysed by two-tailed Student's *t*-test for **b, i**, one-way ANOVA with Šídák's multiple comparisons test for **j**, and log-rank test for **k**. ns, not significant. $P < 0.05$, $*P < 0.01$, $**P < 0.001$.

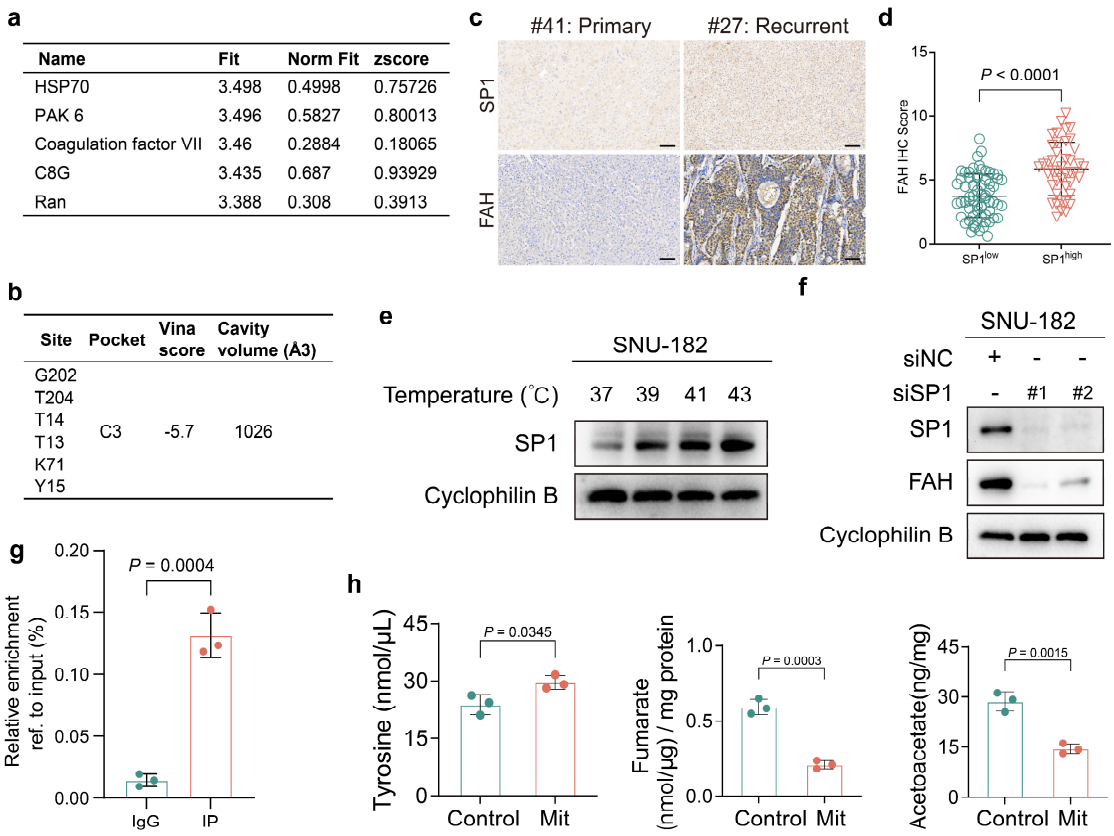

Supplementary Fig. 2 | Increased fumarate induced by SP1-FAH transcriptional regulation binds to and protects HSP70. Related to Fig. 2.

a, Potential fumarate-binding candidates predicted using the PharmMapper Server.

b, Predicted binding pocket between fumarate and HSP70.

c, d, Representative IHC staining of FAH and SP1 in Cohort 3 (**c**), and IHC scores of FAH stratified by SP1 expression levels (**d**). Scale bars, 60 μm.

e, Protein expression levels of SP1 in SNU-182 cells subjected to incremental hyperthermia (37–43 °C). *n* = 3 independent biological replicates.

f, Protein expression levels of FAH in SNU-182 cells following SP1 knockdown. *n* = 3 independent biological replicates.

g, ChIP-qPCR quantification of SP1 binding to the FAH promoter region in SNU-182 cells.

h, Concentrations of tyrosine, fumarate and acetoacetate in SNU-182 cells after SP1 inhibition with mithramycin A (Mit, 1 μM).

Data are presented as mean ± s.d. from *n* biologically independent samples (**d,** *n* = 108; **g, h,** *n* = 3). Statistical significance was analysed by two-tailed Student's *t*-test for **d, g, h**.

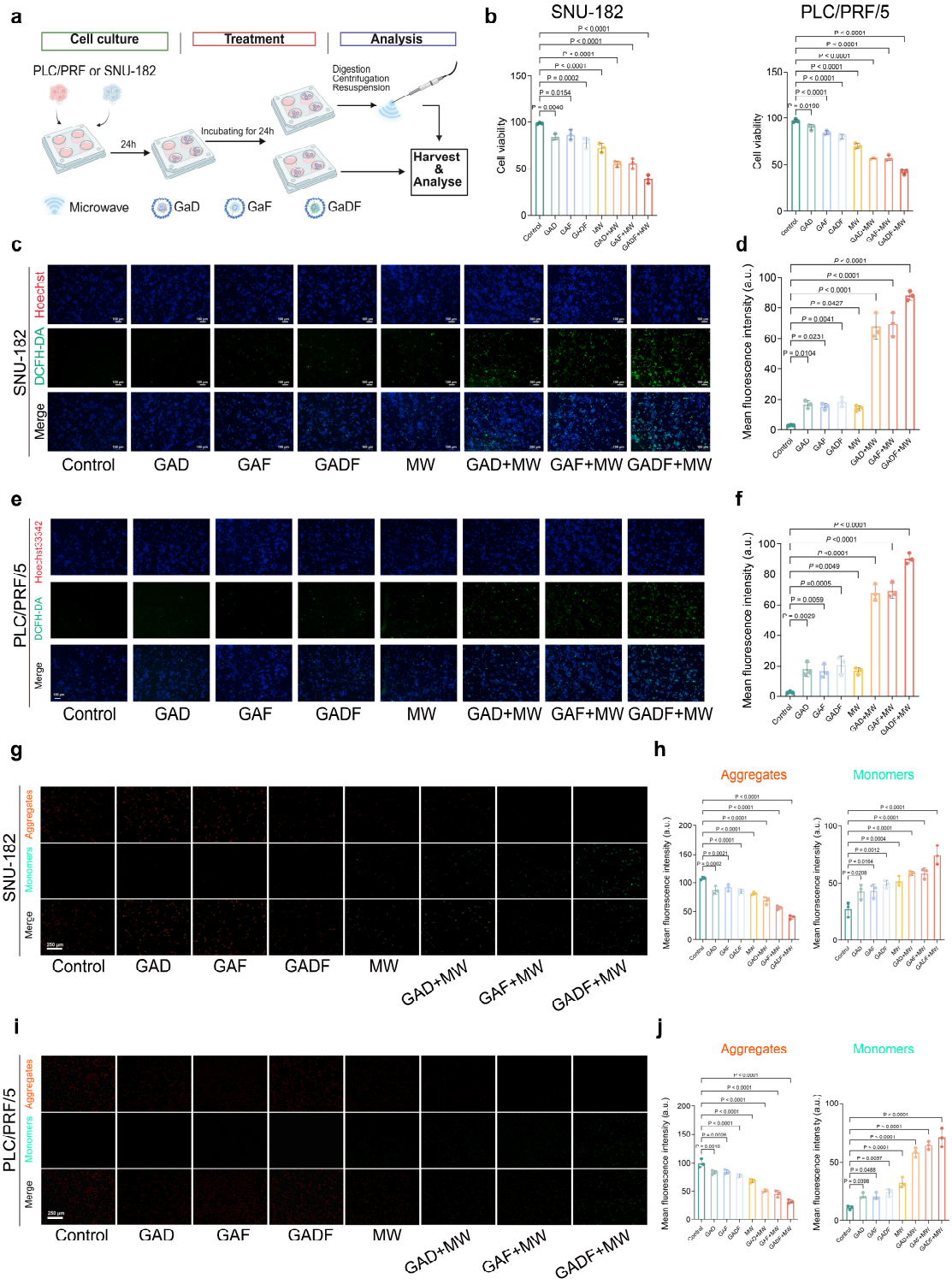

Supplementary Fig. 3 | GADF suppresses tumour growth and combined treatment eradicates HCC cells in vitro. Related to Fig. 3.

a, Schematic of the in vitro validation workflow using SNU-182 and PLC/PRF/5 cell lines. Treatment concentration was 10 μg ml^{-1}. Groups: Control, GAD, GAF, GADF, MW, GAD + MW, GAF + MW, GADF + MW.

b, Cell viability (CCK-8 assay) of SNU-182 and PLC/PRF/5 cells across the indicated groups.

c, Representative DCFH-DA staining images indicating ROS levels in SNU-182 cells across groups. Scale bar, 100 μm. $n = 3$ independent biological replicates.

d, Quantitative analysis of mean DCFH-DA fluorescence intensity in SNU-182 cells.
e, Representative DCFH-DA staining images for ROS in PLC/PRF/5 cells. Scale bar, 100 μm. n = 3 independent biological replicates.
f, Quantitative analysis of mean DCFH-DA fluorescence intensity in PLC/PRF/5 cells.
g, Representative JC-1 fluorescence staining images indicating mitochondrial membrane potential (ΔΨm) in SNU-182 cells; red fluorescence represents JC-1 aggregates (high ΔΨm), green represents monomers (low ΔΨm). Scale bar, 250 μm. n = 3 independent biological replicates.
h, Quantitative analysis of the JC-1 aggregate/monomer ratio in SNU-182 cells.
i, Representative JC-1 staining images for ΔΨm in PLC/PRF/5 cells. Scale bar, 250 μm. n = 3 independent biological replicates.
j, Quantitative analysis of the JC-1 aggregate/monomer ratio in PLC/PRF/5 cells.
Data are presented as mean ± s.d. from n biologically independent samples (**b, d, f, h, j,** n = 3). Statistical significance was analysed by one-way ANOVA with Dunnett's multiple comparisons test versus the control group. Panel **a** created with BioRender.com.

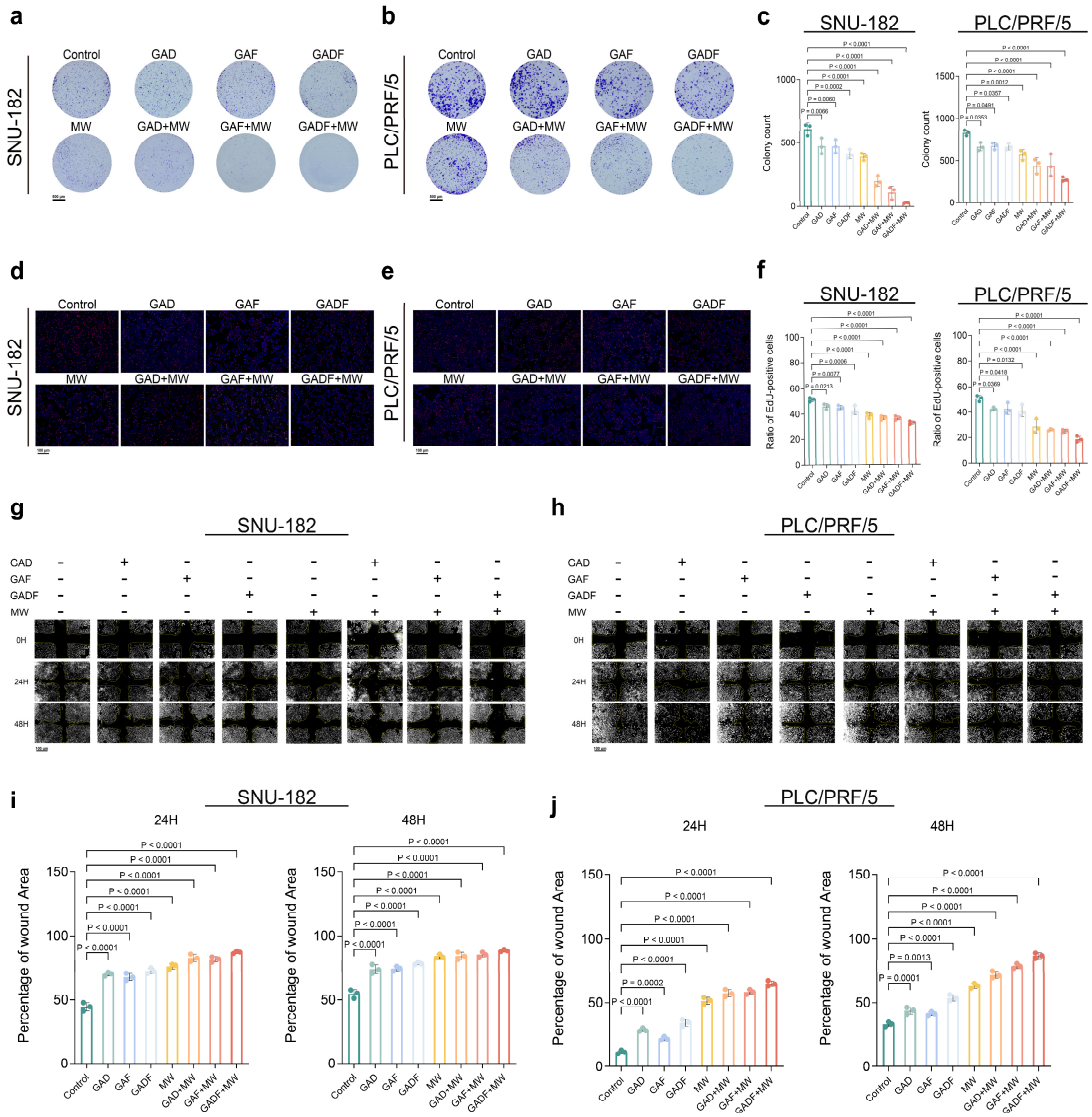

Supplementary Fig. 4 | GADF-based treatment suppresses tumour invasion capabilities in vitro. Related to Fig. 3.

a, b, Representative images of colony formation assays for SNU-182 (**a**) and PLC/PRF/5 (**b**) cells across indicated groups. *n* = 3 independent biological replicates.

c, Quantitative analysis of colony formation numbers.

d, e, Representative EdU staining images of SNU-182 (**d**) and PLC/PRF/5 (**e**) cells. Scale bar, 100 μm. *n* = 3 independent biological replicates.

f, Quantitative analysis of EdU-positive cells.

g, Representative images from wound-healing assays of SNU-182 cells at 0, 24, and 48 h. *n* = 3 independent biological replicates.

h, Representative wound-healing assays of PLC/PRF/5 cells. *n* = 3 independent biological replicates.

i, Quantitative analysis of wound closure area for SNU-182 cells (24 h vs. 0 h, 48 h vs. 24 h).

j, Quantitative analysis of wound closure area for PLC/PRF/5 cells.

Data are presented as mean ± s.d. from *n* biologically independent samples (**c, f, i, j,** *n* = 3). Statistical significance was analysed by one-way ANOVA with Dunnett's multiple comparisons test versus the control group.

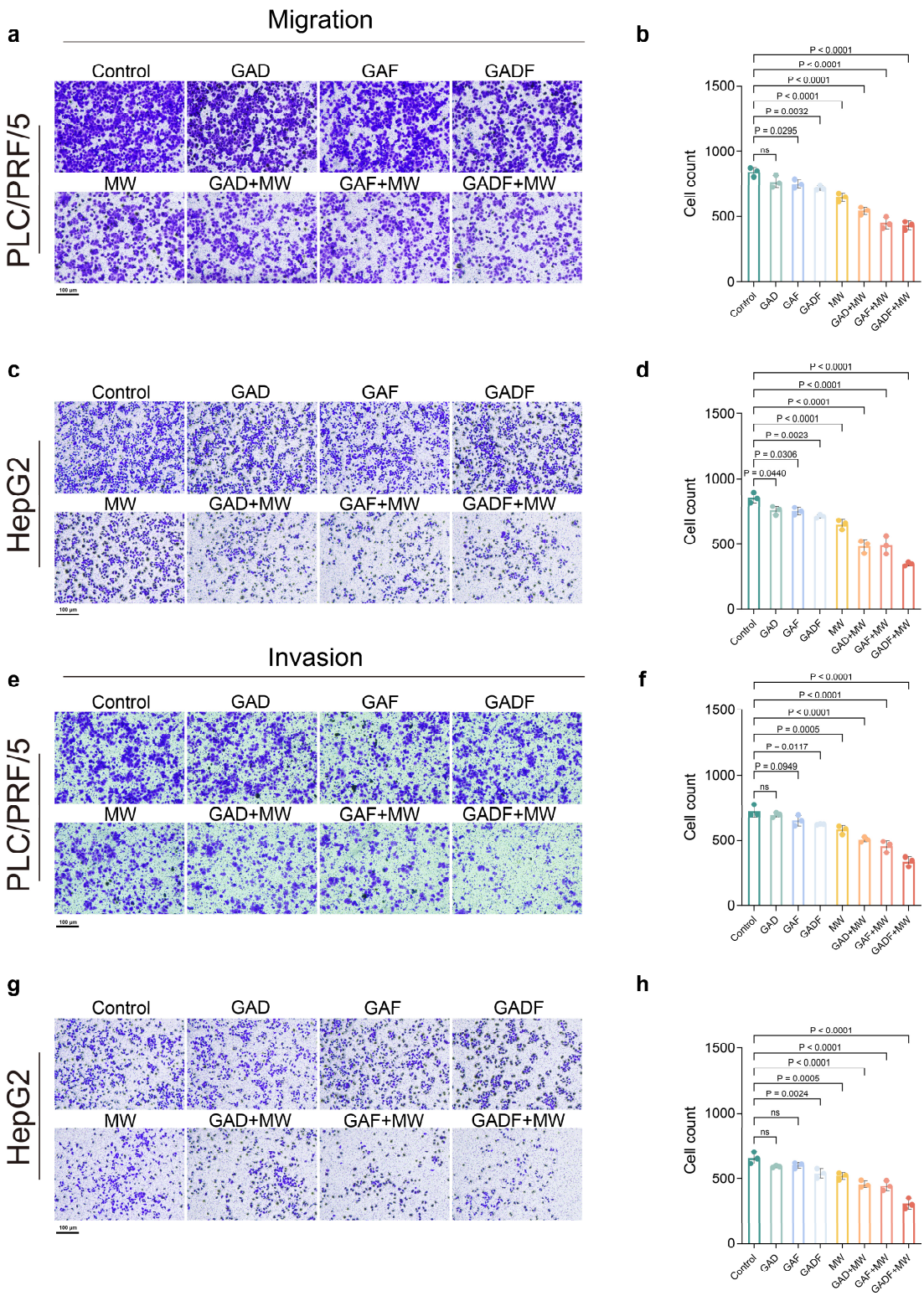

Supplementary Fig. 5 | GADF-based treatment suppresses tumour migration capabilities in vitro. Related to Fig. 3.

a, b, Representative images (**a**) and quantitative analysis (**b**) of migrated PLC/PRF/5 cells. Scale bar, 50 μm. *n* = 3 independent biological replicates.

c, d, Representative images (**c**) and quantification (**d**) of migrated HepG2 cells. Scale bar, 50 μm. *n* = 3 independent biological replicates.

e, f, Representative images (**e**) and quantification (**f**) of invaded PLC/PRF/5 cells. Scale bar, 50 μm. *n* = 3 independent biological replicates.

g, h, Representative images (**g**) and quantification (**h**) of invaded HepG2 cells. Scale bar, 50 μm. *n* = 3 independent biological replicates.

Data are presented as mean ± s.d. from *n* biologically independent samples (**b, d, f, h,** *n* = 3). Statistical significance was analysed by one-way ANOVA with Dunnett's multiple comparisons test versus the control group.

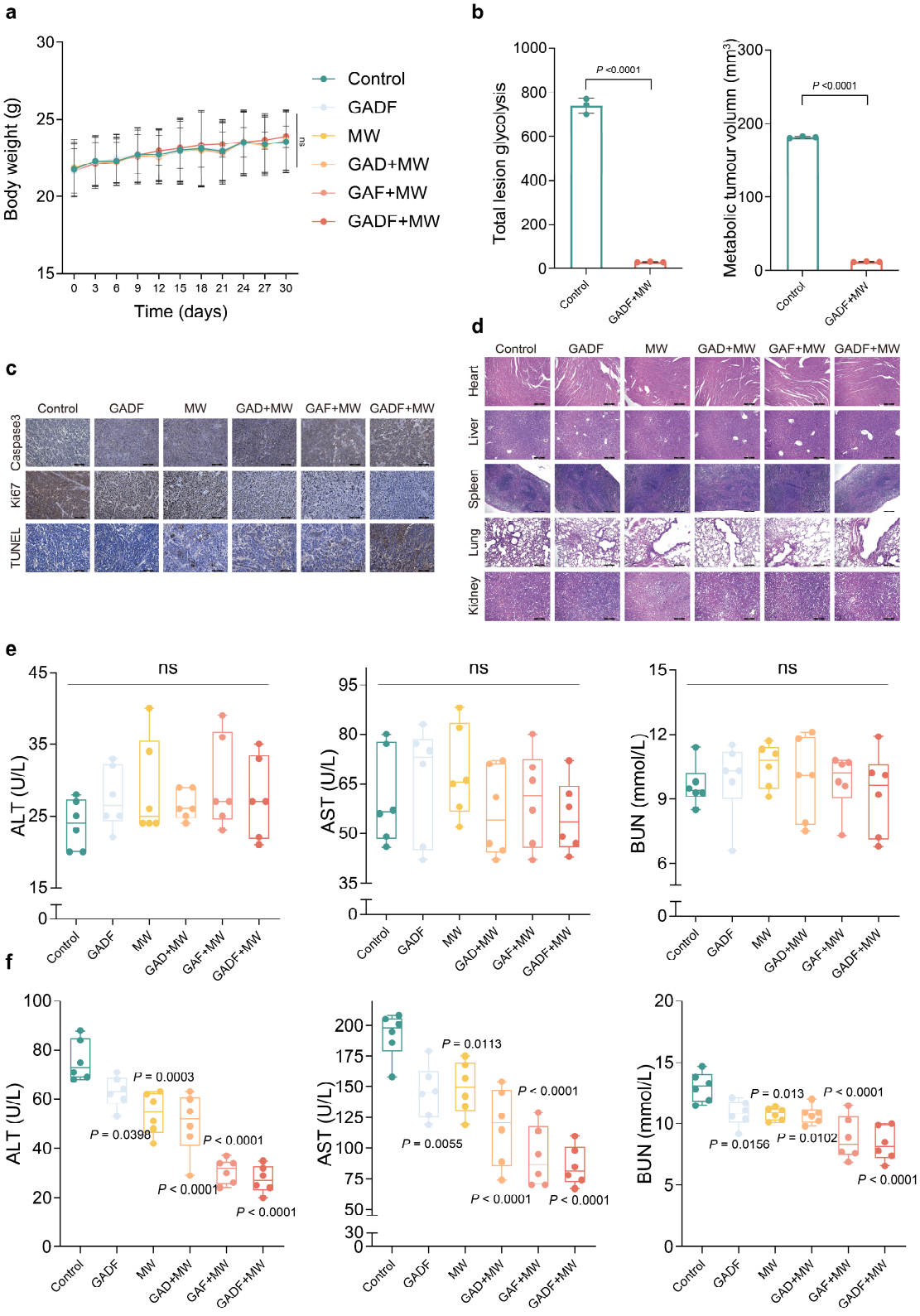

Supplementary Fig. 6 | In vivo therapeutic efficacy and biosafety validation of GADF combined with MW. Related to Fig. 4.

a, Body weight curves of mice from the subcutaneous model (Fig. 4a).

b, Total lesion glycolysis (TLG) and metabolic tumour volume (MTV) for the groups shown in Fig. 4g.

c, Representative IHC staining of caspase-3, Ki-67 and TUNEL in tumours across groups. $n = 6$ mice per group.

d, Representative H&E-stained sections of heart, liver, spleen, lung and kidney tissues. $n = 6$ mice per group.

e, Serum ALT, AST, and BUN levels of mice from the subcutaneous model (Fig. 4a).

f, Serum ALT, AST, and BUN levels of mice from the orthotopic metastasis model (Fig. 4j).

Data are presented as mean ± s.d. from n biologically independent samples (**a, e, f,** $n = 6$; **b,** $n = 3$). Statistical significance was analysed by two-way ANOVA with Dunnett's test for **a**, two-tailed Student's t-test for **b**, and one-way ANOVA with Dunnett's test for **e, f**. Dunnett's test compared each group to the control group. (alanine aminotransferase, ALT; aspartate aminotransferase, AST; blood urea nitrogen, BUN).

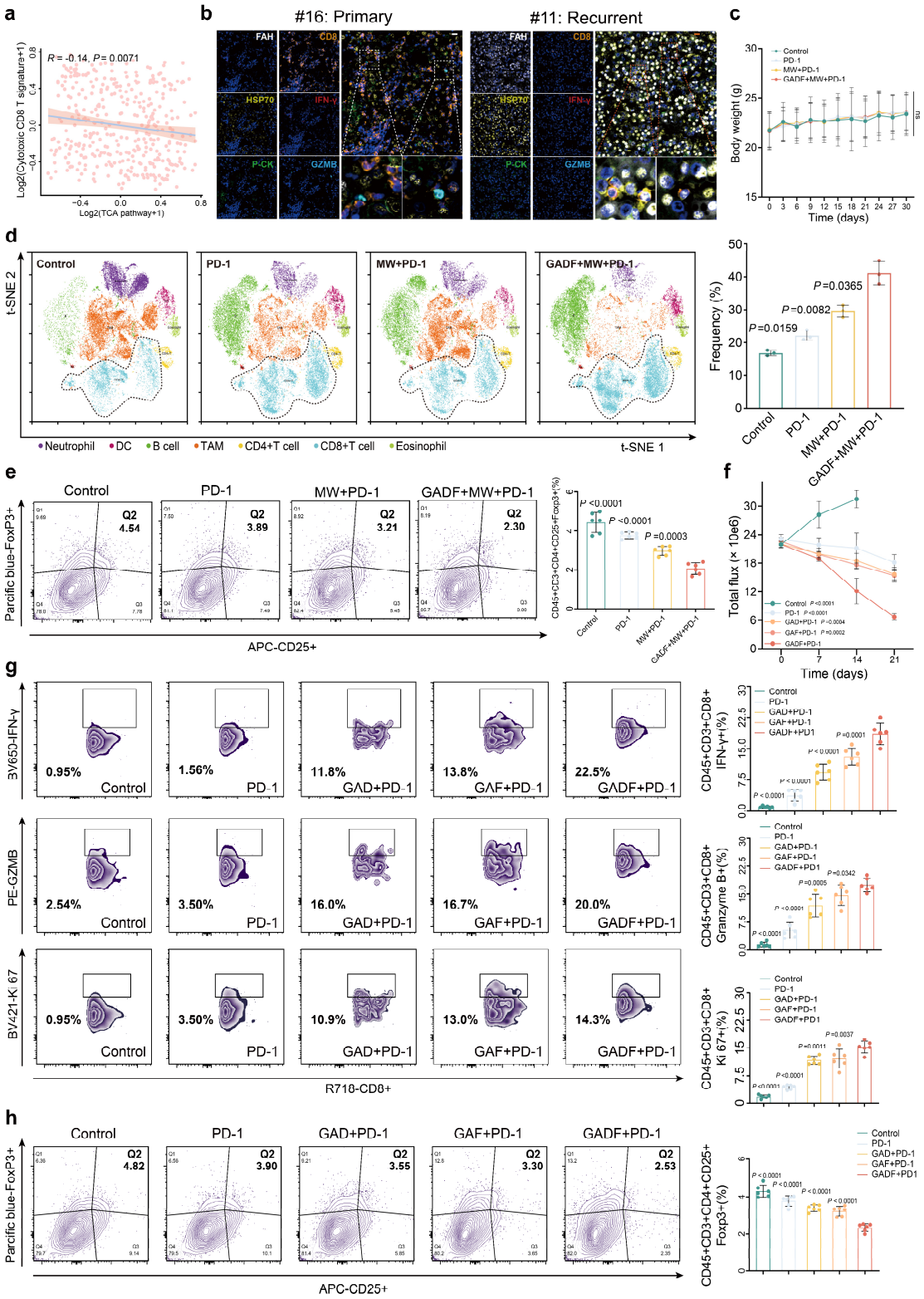

Supplementary Fig. 7 | GADF combinatorial therapy reinvigorates spatial immune landscapes. Related to Fig. 5.

a, Scatter plot showing the Pearson correlation between TCA pathway activity in tumour cells and a cytotoxic CD8⁺ T-cell gene signature in the TCGA-LIHC cohort. Each point represents a patient sample.

b, Representative multiplex immunohistochemistry (mIHC) images showing expression of FAH,

HSP70, pan-cytokeratin (P-CK), CD8, IFN-γ and GZMB in Cohort 1 tissues. Scale bar, 20 μm.
c, Body weight curves for mice bearing distal tumours in the bilateral model (Fig. 5b).
d, t-SNE plots illustrating tumour-infiltrating immune cell profiles and molecule expression for each treatment group. Colours denote $CD8^+$ T cells.
e, Representative flow cytometry plots and quantitative analysis of $FoxP3^+$ $CD4^+$ T cells (Tregs) from distal tumours (Fig. 5b). $n = 3$.
f, Total bioluminescence flux measurements from the pulmonary metastasis model (Fig. 5j) across groups.
g, Representative flow cytometry plots and quantitative analysis of IFN-γ^+, $GZMB^+$, Ki-67^+ $CD8^+$ T cells from the pulmonary metastasis model (Fig. 5j). $n = 6$.
h, Representative flow cytometry plots and quantitative analysis of $FoxP3^+$ $CD4^+$ T cells (Tregs) from Fig. 5j. $n = 6$.
Data are presented as mean ± s.d. from n biologically independent samples (**c, e-h,** $n = 6$; **d,** $n = 3$). Statistical significance was analysed by two-way ANOVA with Dunnett's test for **c**, mixed effect model with Dunnett's multiple comparisons test for **f**, and one-way ANOVA with Dunnett's test for **e, g, h**. ns, not significant. Dunnett's test compared each group to the last group.

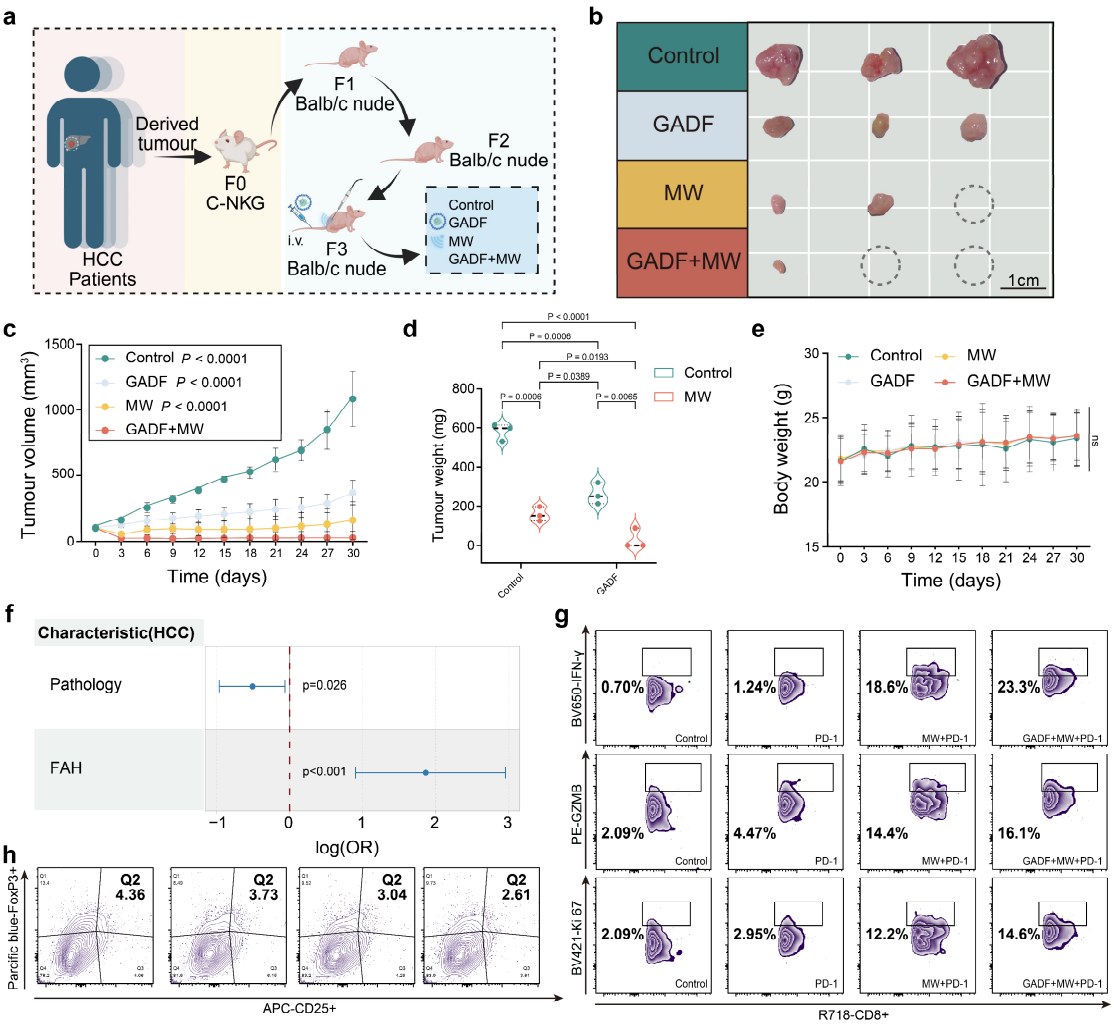

Supplementary Fig. 8 | Therapeutic efficacy of GADF in PDX models and hazard ratios for FAH. Related to Fig. 6.

a, Schematic of the patient-derived xenograft (PDX) model establishment using recurrent HCC tissue from Cohort 2. The F0 generation was engrafted into C-NKG mice, followed by serial passaging into BALB/c nude mice. Groups: Control, GADF, MW, GADF + MW.

b, Representative tumour images from the F3 generation PDX model across groups. $n = 3$ mice per group.

c-e, Tumour volume growth curves (**c**), terminal tumour weights (**d**), and body weight curves (**e**) of F3 PDX mice.

f, Forest plot of hazard ratios for HCC recurrence risk factors based on multivariable Cox proportional hazards regression analysis of Cohort 3.

g, h, Representative flow cytometry plots (**g**) and quantitative analysis (**h**) of IFN-γ$^+$, GZMB$^+$, Ki-67$^+$ CD8$^+$ T cells and FoxP3$^+$ CD4$^+$ T cells from the model in Fig. 6l. $n = 6$ mice per group.

Data are presented as mean ± s.d. from n biologically independent samples (**c, d, e,** $n = 3$; **f,** $n = 108$). Statistical significance was analysed by two-way ANOVA with Dunnett's test for **c, e**, two-way ANOVA with Tukey's test for **d**, and Cox proportional hazards regression model for **f**. ns, not significant. Dunnett's test compared each group to the last group. Normality-compliant groups gave significant ANOVA p-values; violated normality cases showed an overt, complete-regression trend as shown in **c.** Schematic in **a** created with BioRender.com.

Supplementary Table 1 | Association of FAH expression with clinicopathological features of HCC.

	FAH^{high}	FAH^{low}	*P* value	χ^2
All cases	66(61.1%)	42(38.9%)		
Gender				
Female	12(18.2%)	7(16.7%)	0.8402	4.06E-02
Male	54(81.8%)	35(83.3%)		
Age				
>60	37(56.1%)	20(47.6%)	0.43424	0.5099
≤60	29(43.9%)	22(52.4%)		
HBsAg				
Positive	49(74.2%)	33(78.6%)	0.7778	0.079603
Negative	17(25.8%)	9(21.4%)		
HCV				
Positive	4(6.1%)	3(7.1%)	0.8238	4.96E-02
Negative	62(93.9%)	39(92.9%)		
AFP				
>400	12(18.2%)	9(21.4%)	0.868	0.027637
≤400	54(81.8%)	33(78.6%)		
Child-Pugh stage				
A	41(62.1%)	26(61.9%)		
B	24(36.4%)	16(38.1%)	0.7199	0.65734
C	1(1.5%)	0(0.0%)		
BCLC stage				
0	15(22.7%)	4(9.5%)		
A	27(40.9%)	21(50.0%)		
B	22(33.3%)	17(40.5%)	0.2163	-
C	2(3.0%)	0(0.0%)		
Tumour number				
1	52(78.8%)	28(66.7%)		
2	14(21.2%)	13(31.0%)	0.2044	-
3 or more	0(0.0%)	1(2.4%)		
Tumour size (cm)				
>5	9(13.6%)	3(7.1%)	0.4637	0.53693
≤5	57(86.4%)	39(92.9%)		
Pathology				
high	34(51.5%)	32(76.2%)		
middle	1(1.5%)	1(2.4%)	**0.02757**	7.1819
low	31(47%)	9(21.4%)		
Recurrent				
Yes	37(56.1%)	6(14.3%)	**3.76E-05**	16.99
No	29(43.9%)	36(85.7%)		

P values were calculated using the Pearson's chi-square test. A *P* value of <0.05 was considered statistically significant. $n = 108$.

Abbreviations: HBsAg, hepatitis B surface antigen; AFP, alpha-fetoprotein.

Supplementary Table 2 | Univariate and multivariate analyses of factors associated with recurrence in HCC patients.

Variables	Recurrent rate							
	Univariate				Multivariate			
	Coefficient	OR	CI	*P* value	Coefficient	OR	CI	*P* value
FAH	2.0354	7.655314	3.01-22.45	**5.74E-05**	1.8622	6.437885	**2.46-19.20**	0.000315
Gender	0.6342	1.885513	0.69-5.21	0.213				
Age	0.0173	1.017451	0.97-1.07	0.459				
HBV	-0.1361	0.872755	0.36-2.17	0.766				
HCV	1.4218	4.144574	0.85-29.95	0.0989				
AFP	2.34E-05	1.000023	0.999935-1.0001303	0.5804				
Child-Pugh	0.04184	1.042728	0.48-2.23	0.914				
BCLC	-0.0382	0.962511	0.57-1.61	0.884				
Tumour number	-0.09888	0.905851	0.38-2.07	0.817				
Tumour size	-0.05434	0.94711	0.75-1.18	0.634				
Pathology	-0.6493	0.522411	0.34-0.79	**0.00209**	-0.5081	0.601638	**0.38-0.94**	0.025643

Data obtained from the Cox proportional hazards model. A $P < 0.05$ was regarded as statistically significant.

Abbreviations: HBsAg, hepatitis B surface antigen; AFP, alpha-fetoprotein.

Supplementary Table 3 | siRNA/shRNA sequences used in this study.

	Accession	**Target Seg**
sh-FAH (#1)	NM 000137.4	TGAAGTCATCATAACAGGGTA
sh-FAH (#2)	NM 000137.4	GCTACCATATGCAAGTCCAAT
sh-FAH (#3)	NM 000137.4	GAGAGTGTTCTTGCAGAACTT
si-SP1 (#1)	NM_138473.3	AAGCGCUUCAUGAGGAGUGTT
si-SP1 (#2)	NM_138473.3	CCAACAGAUUAUCACAAAUTT
p53-sgRNA	-	CCTCGAGCTCCCTCTGAGCC

The target sequence for p53 knockout was derived from Addgene

https://www.addgene.org/browse/sequence/123311/

Supplementary Table 4 | Information of used antibodies.

Antibodies	Source	Dilution	Identifier
Rabbit anti- FAH polyclonal antibody	Invitrogen	1:400 for mIHC; 0.5 μg/mL for WB; 1:500 for IHC and IF staining	PA5-42049
Mouse anti- HSP70 antibody [5A5]	Abcam	1:1000 for WB; 1:100 for IHC and mIHC; 1:400 for IF staining	ab2787
Rabbit anti-Cyclophilin B Polyclonal Antibody	Invitrogen	1 μg/mL for WB	PA1-027A
Rabbit anti-HMGB1 recombinant antibody	Proteintech	1:300 for IF staining	82973-1-RR
Rabbit anti-calreticulin Polyclonal antibody	Proteintech	1:300 for IF staining	27298-1-AP
Mouse anti-N-cadherin	Proteintech	1:7500 for WB; 1:400 for IF staining	66219-1-Ig
Mouse anti-E-cadherin	Proteintech	1:7500 for WB; 1:400 for IF staining	20874-1-AP
Rabbit anti- human SP1	Abcam	1:5000 for WB; 1:500 for mIHC	ab227383
Cleaved Caspase 3 Polyclonal antibody	Proteintech	1:350 for IHC	25128-1-AP
Ki-67 Polyclonal antibody	Proteintech	1:6000 for IHC	27309-1-AP
CD8α (D8A8Y) Rabbit mAb	Cell Signaling TECHNOLOGY	1:100 for mIHC	85336
Pan-Keratin (C11) Mouse mAb	Cell Signaling TECHNOLOGY	1:100 for mIHC	4545
IFN-γ (D3H2) XP Rabbit mAb	Cell Signaling TECHNOLOGY	1:100 for mIHC	8455
anti- human Granzyme B	Cell Signaling TECHNOLOGY	1:400 for mIHC	17215
HRP-conjugated Goat Anti-Rabbit IgG(H+L)	Proteintech	1:5000 for WB	SA00001-2
HRP-conjugated Goat Anti-Mouse IgG(H+L)	Proteintech	1:5000 for WB	SA00001-1
CoraLite594–conjugated Goat Anti-Rabbit IgG(H+L)	Proteintech	1:300 for IF	SA00013-4
CoraLite488-conjugated Goat Anti-Rabbit IgG(H+L)	Proteintech	1:500 for IF	SA00013-2
Cy3–conjugated Goat Anti-Rabbit IgG(H+L)	Proteintech	1:50 for IF	SA00009-2
BV650 Rat Anti-Mouse IFN-γ	BD Pharmingen	1 μg/mL for FC	563854
PE anti-human/mouse Granzyme B Recombinant	BioLegend	0.5 μg/mL for FC	372208

BV421 Mouse Anti-Ki-67	BD Pharmingen	1 μg/mL for FC	562899
APC-Cy™7 Rat Anti-Mouse CD45	BD Pharmingen	1 μg/mL for FC	557659
FITC Hamster Anti-Mouse CD3e	BD Pharmingen	1 μg/mL for FC	553061
R718 Rat Anti-Mouse CD8a	BD Pharmingen	1 μg/mL for FC	566985
FITC Anti-Mouse CD3e	BioLegend	1 μg/mL for FC	100204
Brilliant Violet 510M Rat Anti-Mouse CD45	BioLegend	0.5 μg/mL for FC	103138
PE/Cyanine Rat Anti-Mouse CD4	BioLegend	0.25 μg/mL for FC	116016
Pacific blue anti-FOXP3	BioLegend	0.5 μg/mL for FC	126410
APC anti-CD25	BioLegend	0.25 μg/mL for FC	112012
In Vivo MAb anti-mouse PD-1 (CD279)	Bioxcell	NA	BE0146
In vivo mAb rat IgG2a isotype control	Bioxcell	NA	BE0089

269

Supplementary Table 5 | Primers for quantitative real-time PCR.

Primers	5' to 3'
β-Tubulin qF	TGGATCCCCAACAATGTCAA
β-Tubulin qR	GGCTGTGCTATTGCCAATGA
FAH qF	CACCTTCCAGCCACCATAGG
FAH qR	CAATTTGGCATCAACGCATT